Title

Toward Stable Cycling of a Cost-Effective Cation-Disordered Rocksalt Cathode via Fluorination

Permalink

Journal

ISSN

Authors

Qian, Ji
Ha, Yang
Koirala, Krishna Prasad
et al.

Publication Date

DOI

Copyright Information

Peer reviewed

Toward Stable Cycling of a Cost-Effective Cation-Disordered Rocksalt Cathode *via* Fluorination

Ji Qian,[a] Yang Ha,[b] Krishna Prasad Koirala,[c] Di Huang,[a] Zhi Huang,[a] Vincent S. Battaglia,[a] Chongmin Wang,[d]

Wanli Yang,[b] and Wei Tong [a,*]

[a] *Energy Storage and Distributed Resources Division, Lawrence Berkeley National Laboratory, Berkeley, CA 94720 USA*

[b] *Advanced Light Source, Lawrence Berkeley National Laboratory, Berkeley, CA 94720 USA*

[c] *Physical and Computational Sciences Directorate, Pacific Northwest National Laboratory, Richland, WA, 99354, USA*

[d] *Environmental Molecular Sciences Laboratory, Pacific Northwest National Laboratory, Richland, WA 99354 USA*

*Correspondence: weitong@lbl.gov

Abstract

The recently developed Li-excess cation-disordered rocksalts (DRXs) exhibit an excellent chemical diversity for the development of alternative Co/Ni-free high-energy cathodes. Herein, we report the synthesis of a highly fluorinated DRX cathode, p, based on cost-effective and earth-abundant transition metals, *via* a solid-state reaction. The fluorinated DRX cathode using ammonium fluoride precursor exhibits more uniform particle size and delivers a specific discharge capacity of 233 mAh g^{-1} and specific energy of 754 Wh kg^{-1}, with 206 mAh g^{-1} retained after 200 cycles. Our combined synchrotron X-ray absorption spectroscopy and resonant inelastic X-ray scattering spectroscopy analysis reveals that the remarkable cycling performance is attributed to the high fluorination and thus enhanced Mn content, enabling the utilization of more Mn redox than the oxide analog. This work demonstrates a great promise to develop next-generation cost-effective DRX cathodes with enhanced capacity retention for high-energy Li-ion batteries.

1. Introduction

Development of new cathode materials with even better performance and lower cost is needed to meet the ever-increasing global demand on lithium-ion batteries. Currently, conventional layered oxides (*e.g.*, $LiNi_{1-x-y}Mn_xCo_yO_2$ (NMC) and $LiNi_{1-x-y}Co_xAl_yO_2$ (NCA), $0 <$ x, y < 1), still remain as the dominating cathodes in commercial lithium-ion batteries for high-energy applications.[1] However, despite their high theoretical capacities (274 mAh g^{-1}), these layered cathodes can only deliver a limited practical capacity (<200 mAh g^{-1}) due to the structural instability at highly delithiated states.[2] Additionally, the state-of-the-art layered cathodes contain a large amount of expensive and scarce transition metals (TMs), *i.e.*, Co and Ni, presenting a formidable barrier to their large-scale applications.[3]

The recently developed Li-excess cation-disordered rocksalts (DRXs) have aroused significant interests owing to their high capacities and structural flexibilities, demonstrating a great potential to address the limitations of layered cathodes.[4] The new family of DRX materials can consistently deliver a high capacity up to 300 mAh g^{-1}, surpassing the state-of-the-art layered cathodes.[5] This high capacity has been achieved through the electrochemical redox of TMs, and anionic oxygen redox for certain materials. The contribution of each redox reaction varies with material composition,[5g, 6] which also affects the electrochemical performance (*e.g.*, capacity, rate, and cycling stability). Unlike the layered cathodes with limited TM choices, DRX structure substantially lessens the elemental constraints and is capable of incorporating a wide variety of TMs as well as fluorine anion at a decent content in the crystal lattice.[5b, 5c, 7] As a result, the dominant TMs have been extended from redox-active Ni and Co to Mn, Fe as well as redox-inactive TM (*e.g.*, Nb, Ti, Zr, Mo) to facilitate the DRX phase formation.[4b, 5d, 8] This exceptional chemical diversity provides unique advantages to tune the material compositions, *i.e.*, stoichiometry of Li and TMs, for optimal performance through the control of redox chemistry.

Moreover, the partial substitution of O by F is feasible in DRX lattice, and less negative F allows the incorporation of more low-valence redox-active TMs without sacrificing the Li content or Li percolation. The approach to improve the utilization of TM redox has been proven to dramatically suppress oxygen loss at high voltages and improve the cycling stability of DRX cathodes.[6d, 7a, 9] Of the many DRX materials reported to date, those composed of cost-effective and earth-abundant TMs, *i.e.*, Mn and Ti, are of particular interest for the development of alternative Co/Ni-free cathodes with improved performance.[5d, 8d, 8j, 10] These two TMs present distinct advantages in cost and resource sustainability compared to their counterparts (*e.g.*, redox-active Co, Ni and redox-inactive Nb, Mo) in conventional layered and other DRX cathodes (**Figure 1a**).[11]

Herein, we report the synthesis of a highly fluoridated Mn-Ti DRX cathode, $Li_{1.2}Mn_{0.6}Ti_{0.2}O_{1.8}F_{0.2}$ (LMTOF), by a solid-state reaction. Besides the conventional LiF, NH_4F is studied as a fluorine precursor in this work, given its lower melting point and higher reactivity than LiF.[12] Additionally, it has been demonstrated that the use of NH_4F can successfully control morphology and particle size in the solid-state reaction.[13] The purpose is to extend the choice of fluorine precursors that could be used for facile control in morphology and particle size, which is essential to develop practical DRX cathodes.[4e] Indeed, the use of NH_4F precursor leads to more uniform particle size and the as-produced LMTOF cathode exhibits remarkable electrochemical performance, as evidenced by an initial discharge capacity of 233 mAh g^{-1} with 200 mAh g^{-1} still accessible after 200 cycles. We thereby investigate the charge compensation mechanism and electrochemical kinetics of the LMTOF cathode upon cycling using advanced spectroscopic and comprehensive electrochemical characterization techniques. This excellent capacity retention is attributed to the utilization of reversible Mn redox that is achieved through the high fluorination, ascertaining that NH_4F is an effective precursor to produce fluorinated DRX material. We believe

this work presents useful insights into further optimization of DRX cathodes, particularly, the development of alternative synthesis for morphology and particle size control for high-energy Li-ion batteries.

2. Results and Discussion

2.1 Synthesis and Electrochemical Performance

LMTOF material is also prepared using LiF for comparison, and it exhibits an identical X-ray diffraction (XRD) pattern to that produced with NH$_4$F precursor, both presenting a typical cubic rocksalt structure with no additional impure phases (**Figure 1b** & **S1a**). The Rietveld refinement reveals a good fit (R_p = 2.38%) with an *a* lattice parameter of 4.1515 Å for the LMTOF material synthesized with NH$_4$F precursor, similar to those (R_p = 2.87%, *a* = 4.1532 Å) obtained with LiF precursor (**Table S1**). Both the as-synthesized LMTOF products have a particle size ranging from a few to tens of micrometers. However, use of NH$_4$F precursor leads to more uniform particle size distribution (**Figure S1b-f**), suggesting NH$_4$F is prone to confine the crystalline growth and promote the formation of regular and uniform particles. For electrochemical characterization, the LMTOF powder is milled with carbon additive to increase the electrical and ionic conductivity by breaking down the particles and achieving homogeneously mixed LMTOF/carbon composites. Therefore, the uniform particle size enables less heterogeneity in redox processes across particles, which is critical to achieve the optimal performance with high capacity and long cycle life. At the particle level, energy-dispersive X-ray spectroscopy (EDS) mapping reveals uniform elemental distribution in both LMTOF electrodes (**Figure 1c** & **Figure S2a**). Atomically-resolved high-angle annular dark field (HAADF) imaging in scanning transmission electron microscope (STEM) (**Figure 1d**) shows that the arrangement of transition metal is consistent with the cubic rocksalt structure, which remains intact on the surface after

milling. The diffuse scattering patterns in the selected area electron diffraction (SAED) (**Figure 1e** & **Figure S2b**) indicate the presence of short-range ordering in pristine LMTOF electrodes prepared with either fluorine precursor.

Furthermore, the LMTOF cathodes prepared by LiF and NH_4F display similar performance, indicating NH_4F is an effective precursor for the synthesis of DRX oxyfluoride cathodes (**Figure S3**). As a result, the detailed characterization is performed on the LMTOF material synthesized with NH_4F. When the material is cycled between 4.8 and 1.5 V, it delivers a specific discharge capacity of 233 mAh g^{-1} with a specific energy of 754 Wh kg^{-1} and energy density of 2985 Wh L^{-1} based on the theoretical density of 3.96 g mL^{-1}. Upon further cycling, this material exhibits a small increase in discharge capacity that reaches up to 251 mAh g^{-1} and remains stable, with 206 mAh g^{-1} retained after 200 cycles (**Figure 2a**). Correspondingly, the average discharge voltage shows an initial drop and stabilizes at ~2.85 V upon extended cycling (**Figure 2b**). It is worth noting that the capacity increase and average voltage decrease mainly occur during the first 20 cycles, correlating well with the structural transformation (to be discussed later). As pointed out earlier, the excellent cycling stability of this LMTOF cathode is attributed to the F substitution for O in DRX crystal lattice, which enables the utilization of more Mn redox during electrochemical cycling, compared to its oxide analog ($Li_{1.2}Mn_{0.4}Ti_{0.4}O_2$). Notably, the F substitution on the O site of $Li_{1.2}Mn_{0.4}Ti_{0.4}O_2$ leads to the overall reduced negative charge per formula unit; to keep the Li stoichiometry unchanged, more low-valence Mn is needed for the charge balance and correct stoichiometry. In principle, Mn^{3+}/Mn^{4+} redox can contribute to a capacity of 193 mAh g^{-1}, accounting for ~83% of the initial capacity. It is noted that the voltage profile (**Figure 2c**) changes from the initial sloping curves to a more flattened one during the early cycles. The evolution of charge-discharge characteristics is more visible in the dQ/dV plots

(**Figure 2d**), which are dominated by two anodic peaks around 3.8 and 4.4 V during the first charge but quickly evolves to 3.0 and 4.0 V after a few charges. Correspondingly, the broad cathodic peak centered at 3.3 V shifts to a strong peak around 2.9 V, leaving the small peak at 4.1 V more noticeable. Note that the 4.1 V cathodic peak appears during the initial discharge and should correlate with the oxidation reaction at higher voltage rather than the new 4.0 V peak that develops later.

Consistent with the previous studies,[10] the newly developed electrochemical features can be attributed to the rocksalt-to-disordered spinel-like phase transformation. The structure of the cycled LMTOF electrodes at the atomic scale is examined by HAADF-STEM (**Figure 3a, c**) and SAED (**Figure 3b, d**). The cubic rocksalt structure remains stable at charged and discharged states after cycling with no observable hole formation as reported on other Li-rich transition metal oxide cathodes. From the SAED pattern, the diffuse scattering pattern associated with short-range ordering disappears, instead, sharp diffraction spots (white box in **Figure 3c**), corresponding to the spinel-like structure, are observed after the 16th charge. Such rocksalt to spinel-like phase transformation is reversible during discharge process as indicated by the disappearance of the spinel-like diffraction spots and reappearance of the features related to short-range ordering recover (**Figure 3d**). The change in the local structure and improved electrochemical performance are consistent with that observed for partial cation-disorder spinel-like phase,[14] which involves the occupancy of Li ions at the tetrahedral sites in the Li-rich compound.[14-15]

2.2 Characterization of Electrochemical Kinetics

Besides the cycling behavior, we further investigate the capacity increase for the LMTOF cathode during early cycles, which is counterintuitive to the commonly observed capacity decay upon high-voltage cycling due to the electrolyte degradation. We thus examine the rate capability

of this material at different current densities (C/20, C/10, C/5, C/2, 1C, 2C), particularly after the structural rearrangement upon cycling. Note that the cell is cycled three times at each rate and detailed analysis is conducted on the third cycle given the stable performance at all rates. The voltage profiles and dQ/dV plots after cycling are presented in **Figure 4**. Before cycling (**Figure S4**), the discharge capacities at C/20, C/10, C/5, C/2, 1C, and 2C are 214, 199, 178, 145, 118, and 92 mAh g^{-1}, respectively (**Figure S3c**). In comparison, the discharge capacity increases after 20 cycles and reaches 243, 220, 194, 158, 129, and 102 mAh g^{-1} at each corresponding rate (**Figure 4a**). The capacity of this material is enhanced after the structural rearrangement. We run the galvanostatic intermittent titration technique (GITT) test after cycling and compare the Li$^+$ kinetics in the disordered and spinel-like phases (**Figure S5**). The improved Li$^+$ kinetics is revealed by comparing the diffusion coefficient at different states of charge, showing the increased diffusion coefficient from about 30% to 60% SOC during charge and from about 70% to 40% SOC during discharge. This result agrees well with the local spinel-like domains formed upon charging. Indeed, the formation of the hybrid structures in the local domains has been observed in other Mn-based cathode materials, and the as-formed heterostructure consistently leads to enhanced electrochemical cycling stability.[16] In the meantime, the rate performance during discharge is also evaluated at a slow charge rate of C/20. Compared to the case with the same charge/discharge rate (**Figure 4a**), slow charge leads to an increase of ~20 mAh g^{-1} in discharge capacities at high rates (**Figure 4c**).

In order to further understand the kinetics of the electrochemical redox reactions, we take a closer look at the change of the anodic/cathodic peaks at different charge/discharge rates. Generally, increasing the charge/discharge current leads to decreased intensity in the anodic peaks around 3.0 and 4.0 V and the cathodic peaks around 2.9 and 4.1 V, accompanied by an increased

polarization (indicated with black arrows in **Figure 4b**). When charged at a slow rate, no obvious polarization is observed for both anodic peaks at 3.0 and 4.0 V. However, comparison between the two anodic peaks at 4.0 and 3.0 V shows a distinct contrast. Regardless of the discharge rate, the 4.0 V anodic peak experiences no change, but the 3.0 V anodic peak decreases with the previous discharge rate (indicated with red arrows in **Figure 4d**). This observation reveals the different kinetics associated with the electrochemical processes at 4.0 and 3.0 V. When charged at a slow rate, the kinetic limitation during charge is largely removed, consistent with the absence of polarization. Therefore, the different charge capacity is mostly related to the available lithium associated with each electrochemical process. We interpret that when the lithium is inserted at a faster rate during the discharge process, lithium preferentially occupies the site that is associated with the 4.0 V oxidation reaction, while the kinetics of the lithiation process for the site related to 3.0 V appears to be slow. When comparing the 3.0 and 4.0 V charge processes at various rates presented in **Figure 4b**, we observe a larger reduction in the 3.0 V anodic peak than the 4.0 V one with increasing the charge rate. Here, we calculate the charge capacities associated with the 3.0 and 4.0 V plateaus in both cases and present the results in **Figure 4e**. The charge capacities are estimated based on the voltages at the inflection points (the lowest values in the dQ/dV charge plots) after the 3.0 and 4.0 V plateaus. The small capacity at the top charge that are sensitive to charge rate is not considered. We focus on the general trend in the charge capacity at each plateau and different rates. As expected, the charge capacity generally decreases with increasing rate (**Figure 4a**), interestingly, this trend does not change when the cell is slowly charged by comparing **Figure 4c** and **Figure 4a**. This is also illustrated by comparing the charge capacities at different plateaus (**Figure 4e**) when the cells are charged at varied rates (marked by red) and slow rate (marked by black) after discharged at varied rates. The fact that the charge capacity does not

increase at a slow charge rate once it is previously discharged at a high rate indicates that the discharge process is rate-limited. Also, as shown in **Figure 4e**, the 3 V plateau charge capacity (marked by squares) displays a remarkable decrease with discharge rate, in a sharp contrast to that at the 4 V plateau (marked by circles), which is less independent of the discharge rate. This rate capability testing points out that the discharge process associated with the 3 V plateau is rate-limited and further understanding of the cause for that will help boost the rate performance of the LMTOF cathode.

2.3 Charge Compensation Mechanism

As evidenced by the electrochemical characterization, a structural rearrangement in LMTOF material is induced upon electrochemical cycling. We thus study the charge compensation mechanism throughout the electrochemical processes using X-ray absorption near edge spectroscopy (XANES) to establish further understanding on the correlation between electrochemical reaction and structural rearrangement. A series states of charge during the 1st and 16th cycle is selected to monitor the oxidation state change of Mn (**Figure 5a**). Note the structural rearrangement takes place after a few cycles so the selected samples are representative for the purpose of this study. The oxidation state of Mn is 3+ at pristine state, upon charging, Mn is oxidized to 4+ at 4.2 V with no further change at higher voltage, suggesting the 4.4 V anodic peak during the first charge is not related to Mn oxidation but rather O oxidation, the detailed characterization will be illustrated in more detail later. During discharge, the reduction of Mn^{4+} initiates below 3.7 V and mostly completes around 2.5 V (**Figure 5b, c**). Based on the XANES results, the anodic reaction at 3.8 V and cathodic reaction around 3.3 V during the 1st cycle are associated with Mn redox. After cycling, the oxidation process is featured by 3.0 and 4.0 V anodic peaks while the reduction process is dominated by the 2.9 V cathodic peak along with the 4.1 V

one. During the 16th cycle, Mn oxidation continues until 4.5 V charge, and its reduction consistently starts below 3.7 V during discharge (**Figure 5d, e**). We thereby infer that the small cathodic peak at 4.1 V, which is present during the initial discharge but becomes more invisible after several discharges, is associated with the O reduction. The increased reduction peak intensity could presumably be attributed to the improved Li$^+$ kinetics in the spinel-like phase as discussed previously. Throughout the charge and discharge processes, the Mn K pre-edge features are dominated by two peaks at 6541.3 and 6543.1 eV (insets in **Figure 5b, d**), similar to those observed on Li-rich layered oxides and NMC cathodes.[17] Overall, the Mn-K XANES spectra only display subtle pre-edge changes at different states of charge, suggesting minor geometric changes at the Mn site. Clearly, the newly developed electrochemical oxidation at 3.0 and 4.0 V and reduction at 2.9 V are associated with Mn redox.

In addition to the Mn redox that is analyzed above through hard X-ray absorption spectroscopy (XAS), soft X-ray resonant inelastic X-ray scattering spectroscopy (RIXS) measurements are conducted to investigate the participation of O redox in the electrochemistry. RIXS map of the first fully charged sample shows the characteristic feature of the oxidized O at the excitation energy of ~531 eV and emission energy of ~524 eV (red arrow in **Figure 6a**), confirming the participation of O redox at high voltages in the LMTOF material,[18] given no further Mn oxidation above 4.2 V. Such an oxidized O feature remains visible in the charged electrode after 16 cycles, although the intensity decays upon cycling. In contrast, this feature disappears in the discharged electrode (**Figure 6b**), indicating a reversible lattice oxygen redox reaction. The reversible spectral evolution associated with the O redox reaction can be better visualized *via* a direct comparison of the individual RIXS cuts at the characteristic 531 eV excitation energy, which shows the appearance and disappearance of the peak at ~524 eV emission

energy at charged and discharged states, respectively (guided by the dashed line in **Figure 6c**). Combined with the Mn XANES results, it can be concluded that a finite amount of O redox reaction (although not quantifiable) participates in the electrochemical reaction at high voltages, but the overall charge compensation is predominated by the Mn redox. Moreover, the structural rearrangement does not affect the redox mechanism, but it modifies the (de)lithiation mechanism.

As revealed by the previous study, the emerging electrochemical features after cycling show some consistency with those of spinel-like phase, as observed by the two distinct charge plateaus at 4.0 and 3.0 V.[10, 15] In conventional spinel phase, Li and Mn ions are located at tetrahedral 8(a) and octahedral 16(d) sites, respectively. As such, the electrochemical process associated with the tetrahedral Li and octahedral Mn takes place around 4 V.[19] Given the nature of Li excess, it is likely that Li occupies the octahedral sites in the LMTOF material when the tetrahedral sites are full. The LiO_4 tetrahedron is much smaller than the LiO_6 octahedron, and the insertion and extraction of Li^+ into and from the oxygen tetrahedra and octahedra result in different changes in the Gibbs free energy, thus the electrochemical potentials.[20] The octahedrally coordinated Li could account for the low-voltage plateau at 3.0 V.[21] It is worth noting that the atomic arrangement (e.g., ordering/disordering) can modify the electrochemical potential by changing the site energy and/or local atomic environment.[20] Our rate capability study indicates that the electrochemical reaction associated with 3.0 V charge plateau is rate-limiting, as opposed to the 4.0 V charge plateau. Interestingly, compared to the charge process, the voltage profile of this LMTOF material during discharge is asymmetric, which is notably dominated by an extended plateau at 2.9 V. As discussed previously, the 4.1 V cathodic peak is associated with the O reduction, corresponding to an oxidation reaction at even higher charge voltage. The very different charge-discharge potentials may originate from the varied cation distribution during charge and

discharge. And the asymmetric charge-discharge profiles could be an indication of a dynamic process accompanied by cation redistribution upon (de)lithiation. Although the detailed mechanism requires further investigation, it can be seen from the electrochemical studies that this dynamic process is highly reversible upon extended cycling.

3. Conclusion

A highly fluorinated DRX material, $Li_{1.2}Mn_{0.6}Ti_{0.2}O_{1.8}F_{0.2}$, composed of cost-effective and earth-abundant Mn and Ti, is synthesized *via* a solid-state reaction. We have demonstrated the dual role of NH_4F as both fluorine source and particle size control additive. The as-produced LMTOF cathode exhibits more uniform particle size and thus promising electrochemical performance with an initial discharge capacity of 233 mAh g^{-1} (energy density of 754 Wh kg^{-1} and 2985 Wh L^{-1} based on the theoretical density of 3.96 g mL^{-1}). It also displays remarkable cycling stability, with 206 mAh g^{-1} capacity retained after 200 cycles (88.4% capacity retention). Such excellent cycling performance is mostly achieved through the utilization of reversible Mn redox enabled by high fluorination. Upon cycling, this fluorinated DRX cathode with enhanced Mn content experiences local structural rearrangement that does not modify the redox mechanism but the (de)lithiation mechanism with differed electrochemical kinetics. This work reports the recent advancement in developing cost-effective DRX cathodes with enhanced cycling performance for high-energy Li-ion batteries. It also demonstrates that NH_4F is an effective precursor, which essentially addresses the limited choices of fluorine precursors for fluorinated DRX synthesis through solution chemistry for control of morphology and particle size.

4. Experimental Methods

Synthesis and Physical Characterization: LMTOF materials are prepared by a solid-state reaction. Thoroughly mixed precursors (lithium carbonate (Li_2CO_3), manganese oxide (Mn_2O_3),

titanium oxide (TiO_2), and lithium fluoride (LiF) or ammonium fluoride (NH_4F)) are annealed at 1030 °C for 4 h under Ar atmosphere. To compensate for Li loss at high temperature, 10% Li excess is added through the Li_2CO_3 precursor. XRD patterns are collected on a Bruker D2-Phaser with Cu Kα radiation (λ = 1.54178 Å). Scanning electron microscopy (SEM) is conducted on a JEOL JSM-7000F equipped with a Thermo Scientific EDS detector. Electron diffraction studies are performed on an aberration-corrected FEI Titan 80-300 S/TEM microscope operated at 300 kV. SEAD patterns are taken with a 10 μm aperture and processed using Digital Micrograph software (Gatan). Atomically resolved HAADF-STEM images and EDS data acquisition are conducted on a Thermo-Fisher Themis-Z S/TEM operated at 300 kV. The probe convergence angle is set at 24.8 mrad and the inner detection angle on the HAADF detector is 3 times higher than the probe convergence angle. The EDS data are processed using the software "Velox", where the overlapped peaks are deconvoluted by using the stored standard reference spectra and employing a Filtered Least Squares (FLS) method to fit the peaks and remove the background. For the particle size analysis, the DRX powders were dispersed in isopropanol at a concentration of 0.001 wt% by a homogenizer (IKA T25) and then measured with a particle size analyzer (Malvern Mastersizer 3000).

XAS and RIXS: Hard XAS measurements are conducted at the Beamline 2-2 at Stanford Synchrotron Radiation Lightsource (SSRL). *Ex situ* LMTOF electrodes are harvested when the cells reach their designated states of charge, then rinsed by dimethyl carbonate solvent and dried inside an Ar-filled glovebox. Si (220) crystal is applied as a monochromator. XANES data are analyzed using SIXPACK software. RIXS maps are collected in the ultra-high efficiency iRIXS endstation at Beamline 8.0.1 at the Advanced Light Sources (ALS). All samples are sealed in a home-made sample transfer kit inside an Ar-filled glove box, then transferred and coupled to the

iRIXS vacuum system without exposure to air. The sample surface is mounted at 45° to the incident beam, and the outgoing photon direction along the RIXS spectrograph is 90°. The resolution of the excitation energy is about 0.2 eV and the emission energy about 0.35 eV. An excitation energy step size of 0.2 eV was used for all maps. All of the spectra are normalized to the beam flux measured by the upstream gold mesh, and RIXS spectra are also normalized to the collection time for each individual cut.

Electrochemical Characterization: LMTOF powder and acetylene carbon black (Denka, 50% compressed) are sufficiently milled, then mixed with polyvinylidene fluoride dissolved in N-methylpyrrolidone solvent to obtain a uniform slurry of LMNOF: acetylene black: PVdF (70:20:10, wt%). The slurry is cast on an aluminum foil using a doctor blade and then dried under vacuum at 120 °C for 12 h. The punched electrode is assembled in a 2032-type coin cell along with Li metal foil, Celgard 2400 separator, and 1 M $LiPF_6$ in 1:2 w/w ethylene carbonate / diethyl carbonate inside an Ar-filled glovebox. The active material loading is ~2.5 mg cm^{-2}. The galvanostatic charge-discharge cycling is performed on an Arbin battery testing station. 1 C capacity is defined as 321 mAh g^{-1}. GITT measurements are conducted after galvanostatic charge/discharge at C/20 for 20 cycles. After that, the cell is rested for 8 h after every 1.5 h during the charge/discharge at C/20 between 1.5 and 4.8 V. The diffusion coefficient is proportional to the $(\Delta E_s / \Delta E_t)^2$ value based on the equation: $D = \frac{4}{\pi t} \left(\frac{m_B V_M}{M_B S} \right)^2 \left(\frac{\Delta E_s}{\Delta E_\tau} \right)^2$, where t is the pulse duration, m_B and M_B are the active mass and molar mass, V_M is the molar volume, and S is the active surface area of LMTOF electrode. The $(\Delta E_s / \Delta E_t)^2$ value is thus used to evaluate the Li$^+$ kinetics at different states of charge in the LMTOF cathode after cycling.

Supporting Information

Supporting Information is available from the Wiley Online Library or from the author.

Acknowledgements

Conflict of Interest

The authors declare no conflict of interest.

Data Availability Statement

The data that support the findings of this study are available from the corresponding author upon reasonable request.

References

[1]   a) M. S. Whittingham, *Chem. Rev.* **2004**, *104*, 4271; b) J. Xu, F. Lin, M. M. Doeff, W. Tong, *J. Mater. Chem. A* **2017**, *5*, 874.

[2]   a) J. Xu, E. Hu, D. Nordlund, A. Mehta, S. N. Ehrlich, X.-Q. Yang, W. Tong, *ACS Applied Materials & Interfaces* **2016**, *8*, 31677; b) N. Li, S. Sallis, J. K. Papp, B. D. McCloskey, W. Yang, W. Tong, *Nano Energy* **2020**, *78*, 105365.

[3]   E. A. Olivetti, G. Ceder, G. G. Gaustad, X. Fu, *Joule* **2017**, *1*, 229.

[4]   a) J. Lee, A. Urban, X. Li, D. Su, G. Hautier, G. Ceder, *Science* **2014**, *343*, 519; b) N. Yabuuchi, M. Takeuchi, M. Nakayama, H. Shiiba, M. Ogawa, K. Nakayama, T. Ohta, D. Endo, T. Ozaki, T. Inamasu, *PNAS* **2015**, *112*, 7650; c) R. Clément, Z. Lun, G. Ceder, *Energy & Environmental Science* **2020**, *13*, 345; d) D. Chen, J. Ahn, G. Chen, *ACS Energy Lett.* **2021**, *6*, 1358; e) H. Li, R. Fong, M. Woo, H. Ahmed, D.-H. Seo, R. Malik, J. Lee, *Joule* **2022**, *6*, 53.

[5]   a) J. Lee, D.-H. Seo, M. Balasubramanian, N. Twu, X. Li, G. Ceder, *Energy Environ. Sci.* **2015**, *8*, 3255; b) J. Lee, J. K. Papp, R. J. Clément, S. Sallis, D.-H. Kwon, T. Shi, W. Yang, B. D. McCloskey, G. Ceder, *Nat. Commun.* **2017**, *8*, 981; c) J. Lee, D. A. Kitchaev, D.-H. Kwon, C.-W. Lee, J. K. Papp, Y.-S. Liu, Z. Lun, R. J. Clément, T. Shi, B. D. McCloskey, J. Guo, M. Balasubramanian, G. Ceder, *Nature* **2018**, *556*, 185; d) H. Ji, A. Urban, D. A. Kitchaev, D.-H. Kwon, N. Artrith, C. Ophus, W. Huang, Z. Cai, T. Shi, J. C. Kim, H. Kim, G. Ceder, *Nat. Commun.* **2019**, *10*, 592; e) Z. Lun, B. Ouyang, Z. Cai, R. J. Clément, D.-H. Kwon, J. Huang, J. K. Papp, M. Balasubramanian, Y. Tian, B. D. McCloskey, H. Ji, H. Kim, D. Kitchaev, G. Ceder, *Chem* **2020**, *6*, 153; f) Z. Cai, H. Ji, Y. Ha, J. Liu, D.-H. Kwon, Y. Zhang, A. Urban, E. E. Foley, R. Giovine, H. Kim, Z. Lun, T.-Y. Huang, G. Zeng, Y. Chen, J. Wang, B. D. McCloskey, M. Balasubramanian, R. J. Clément, W. Yang, G. Ceder, *Matter* **2021**, *4*, 3897; g) Z. Lun, B. Ouyang, D.-H. Kwon, Y. Ha, E. E. Foley, T.-Y. Huang, Z. Cai, H. Kim, M. Balasubramanian, Y. Sun, J. Huang, Y. Tian, H. Kim, B. D. McCloskey, W. Yang, R. J. Clément, H. Ji, G. Ceder, *Nat. Mater.* **2021**, *20*, 214.

[6]   a) M. J. Crafton, Y. Yue, T.-Y. Huang, W. Tong, B. D. McCloskey, *Adv. Energy Mater.* **2020**, *10*, 2001500; b) T.-Y. Huang, M. J. Crafton, Y. Yue, W. Tong, B. D. McCloskey, *Energy Environ. Sci.* **2021**, *14*, 1553; c) Y. Yue, Y. Ha, T.-Y. Huang, N. Li, L. Li, Q. Li, J. Feng, C. Wang, B. D. McCloskey, W. Yang, W. Tong, *ACS Nano* **2021**, *15*, 13360; d) Y. Yue, N. Li, Y. Ha, M. J. Crafton, B. D. McCloskey, W. Yang, W. Tong, *Adv. Funct. Mater.* **2021**, *31*, 2008696.

[7]   a) Z. Lun, B. Ouyang, D. A. Kitchaev, R. J. Clément, J. K. Papp, M. Balasubramanian, Y. Tian, T. Lei, T. Shi, B. D. McCloskey, J. Lee, G. Ceder, *Adv. Energy Mater.* **2019**, *9*, 1802959; b) W. D. Richards, S. T. Dacek, D. A. Kitchaev, G. Ceder, *Adv. Energy Mater.* **2018**, *8*, 1701533.

[8]   a) S. L. Glazier, J. Li, J. Zhou, T. Bond, J. Dahn, *Chem. Mater.* **2015**, *27*, 7751; b) R. Wang, X. Li, L. Liu, J. Lee, D.-H. Seo, S.-H. Bo, A. Urban, G. Ceder, *Electrochem. Commun.* **2015**, *60*, 70; c) A. Kitajou, K. Tanaka, H. Miki, H. Koga, T. Okajima, S. Okada, *Electrochemistry* **2016**, *84*, 597; d) N. Yabuuchi, M. Nakayama, M. Takeuchi, S. Komaba, Y. Hashimoto, T. Mukai, H. Shiiba, K. Sato, Y. Kobayashi, A. Nakao, *Nat. Commun.* **2016**, *7*, 13814; e) N. Yabuuchi, Y. Tahara, S. Komaba, S. Kitada, Y. Kajiya, *Chem. Mater.* **2016**, *28*, 416; f) N. Yabuuchi, M. Takeuchi, S. Komaba, S. Ichikawa, T. Ozaki, T. Inamasu, *Chem. Commun.* **2016**, *52*, 2051; g) S. Hoshino, A. M. Glushenkov, S. Ichikawa, T. Ozaki, T. Inamasu, N. Yabuuchi, *ACS Energy Lett.* **2017**, *2*, 733; h) N. Takeda, S. Hoshino, L. Xie, S. Chen, I. Ikeuchi, R. Natsui, K. Nakura, N. Yabuuchi, *J. Power Sources* **2017**, *367*, 122; i) N. Takeda, I. Ikeuchi, R. Natsui, K. Nakura, N. Yabuuchi, *ACS Appl. Energy Mater.* **2019**, *2*, 1629; j) Y. Kobayashi, M. Sawamura, S. Kondo, M. Harada, Y. Noda, M. Nakayama, S. Kobayakawa, W. Zhao, A. Nakao, A. Yasui, H. B. Rajendra, K. Yamanaka, T. Ohta, N. Yabuuchi, *Mater. Today* **2020**, *37*, 43; k) W. H. Kan, D. Chen, J. K. Papp, A. K. Shukla, A. Huq, C. M. Brown, B. D. McCloskey, G. Chen, *Chem. Mater.* **2018**, *30*, 1655; l) D. Chen, J. Ahn, E. Self, J. Nanda, G. Chen, *J. Mater. Chem. A* **2021**, *9*, 7826.

[9]   a) J. Lee, C. Wang, R. Malik, Y. Dong, Y. Huang, D.-H. Seo, J. Li, *Adv. Energy Mater.* **2021**, *11*, 2100204; b) K. Zhou, S. Zheng, F. Ren, J. Wu, H. Liu, M. Luo, X. Liu, Y. Xiang, C. Zhang, W. Yang, L. He, Y. Yang, *Energy Stor. Mater.* **2020**, *32*, 234.

[10]   L. Li, Z. Lun, D. Chen, Y. Yue, W. Tong, G. Chen, G. Ceder, C. Wang, *Adv. Funct. Mater.* **2021**, *31*, 2101888.

[11]   Wikipedia,   Prices   of   Chemical   Elements, https://en.wikipedia.org/wiki/Prices_of_chemical_elements, accessed: April, **2022**.

[12]   J. Chun, C. Jo, S. Sahgong, M. G. Kim, E. Lim, D. H. Kim, J. Hwang, E. Kang, K. A. Ryu, Y. S. Jung, Y. Kim, J. Lee, *ACS Appl. Mater. Interfaces* **2016**, *8*, 35180.

[13]   L. Zhu, C. Sun, L. Chen, X. Lu, S. Li, G. Ye, L. Liu, *Z. Naturforsch. B* **2017**, *72*, 665.

[14]   Y. Pei, Q. Chen, M. Wang, P. Zhang, Q. Ren, J. Qin, P. Xiao, L. Song, Y. Chen, W. Yin, X. Tong, L. Zhen, P. Wang, C.-Y. Xu, *Nat. Commun.* **2022**, *13*, 6158.

[15]   Y. Yue, N. Li, L. Li, E. E. Foley, Y. Fu, V. S. Battaglia, R. J. Clément, C. Wang, W. Tong, *Chem. Mater.* **2020**, *32*, 4490.

[16]   a) H. Xia, X. Zhu, J. Liu, Q. Liu, S. Lan, Q. Zhang, X. Liu, J. K. Seo, T. Chen, L. Gu, Y. S. Meng, *Nat. Commun.* **2018**, *9*, 5100; b) X. Zhu, F. Meng, Q. Zhang, L. Xue, H. Zhu, S. Lan, Q. Liu, J. Zhao, Y. Zhuang, Q. Guo, B. Liu, L. Gu, X. Lu, Y. Ren, H. Xia, *Nat. Sustain.* **2021**, *4*, 392.

[17]   a) J. R. Croy, H. Iddir, K. Gallagher, C. S. Johnson, R. Benedek, M. Balasubramanian, *Phys. Chem. Chem. Phys.* **2015**, *17*, 24382; b) W.-S. Yoon, M. Balasubramanian, K. Y. Chung, X.-Q. Yang, J. McBreen, C. P. Grey, D. A. Fischer, *J. Am. Chem. Soc.* **2005**, *127*, 17479; c) M. J. Zuba, A. Grenier, Z. Lebens-Higgins, G. J. P. Fajardo, Y. Li, Y. Ha, H. Zhou, M. S. Whittingham, W. Yang, Y. S. Meng, K. W. Chapman, L. F. J. Piper, *ACS Energy Lett.* **2021**, *6*, 1055.

[18]   W. Yang, T. P. Devereaux, *J. Power Sources* **2018**, *389*, 188.

[19]   D. Tang, L. Ben, Y. Sun, B. Chen, Z. Yang, L. Gu, X. Huang, *J. Mater. Chem. A* **2014**, *2*, 14519.

[20]   C. Liu, Z. G. Neale, G. Cao, *Mater. Today* **2016**, *19*, 109.

[21]   B. Shi, J. Gim, L. Li, C. Wang, A. Vu, J. R. Croy, M. M. Thackeray, E. Lee, *Chem. Commun.* **2021**, *57*, 11009.
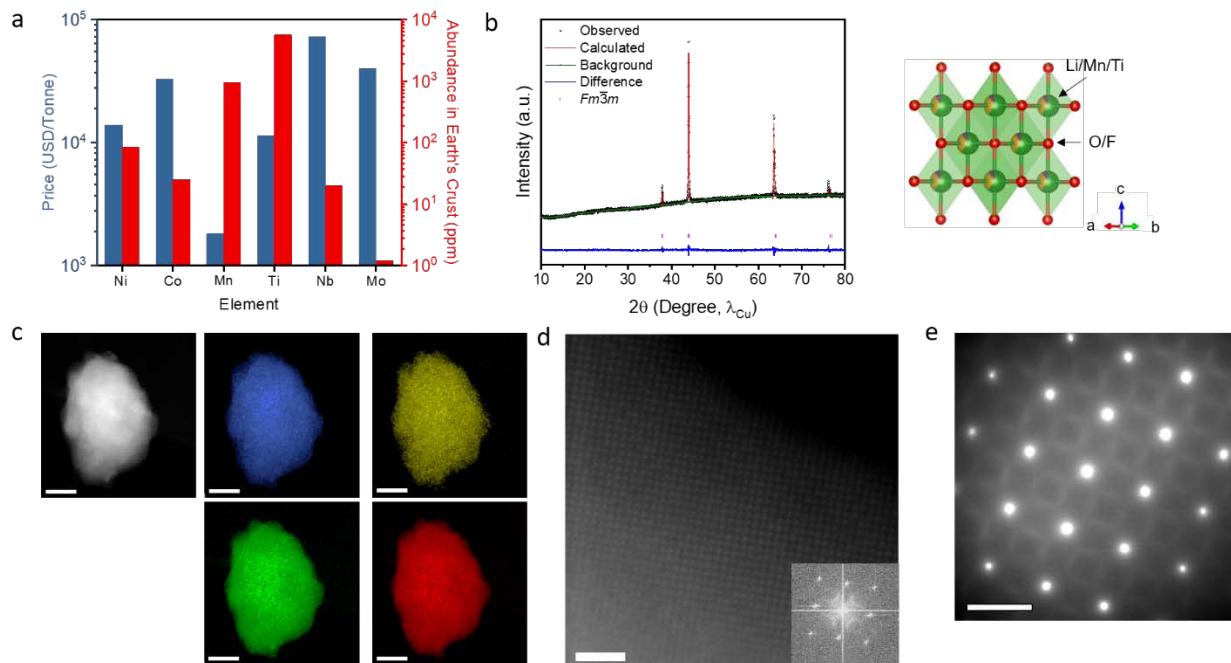
Figure 1. Structural characterization of LMTOF material prepared with NH$_4$F precursor. (a) Cost and earth abundance analysis of the representative transition metals in DRX cathodes;[11] (b) XRD pattern and Rietveld refinement analysis based on $Fm\bar{3}m$ (a = 4.1515 Å, R_p = 2.38%), the schematic shows the arrangement of cations and anions in the disordered rocksalt structure; (c) EDS maps of Mn (blue), Ti (yellow), O (green), and F (red); (d) representative HAADF-STEM image and inset fast Fourier transforms (FFT); and (e) SEAD pattern, showing disordered rocksalt structure with short-range ordering. The scale bar in (c), (d), and (e) is 200 nm, 1 nm, and 5 nm^{-1}, respectively.
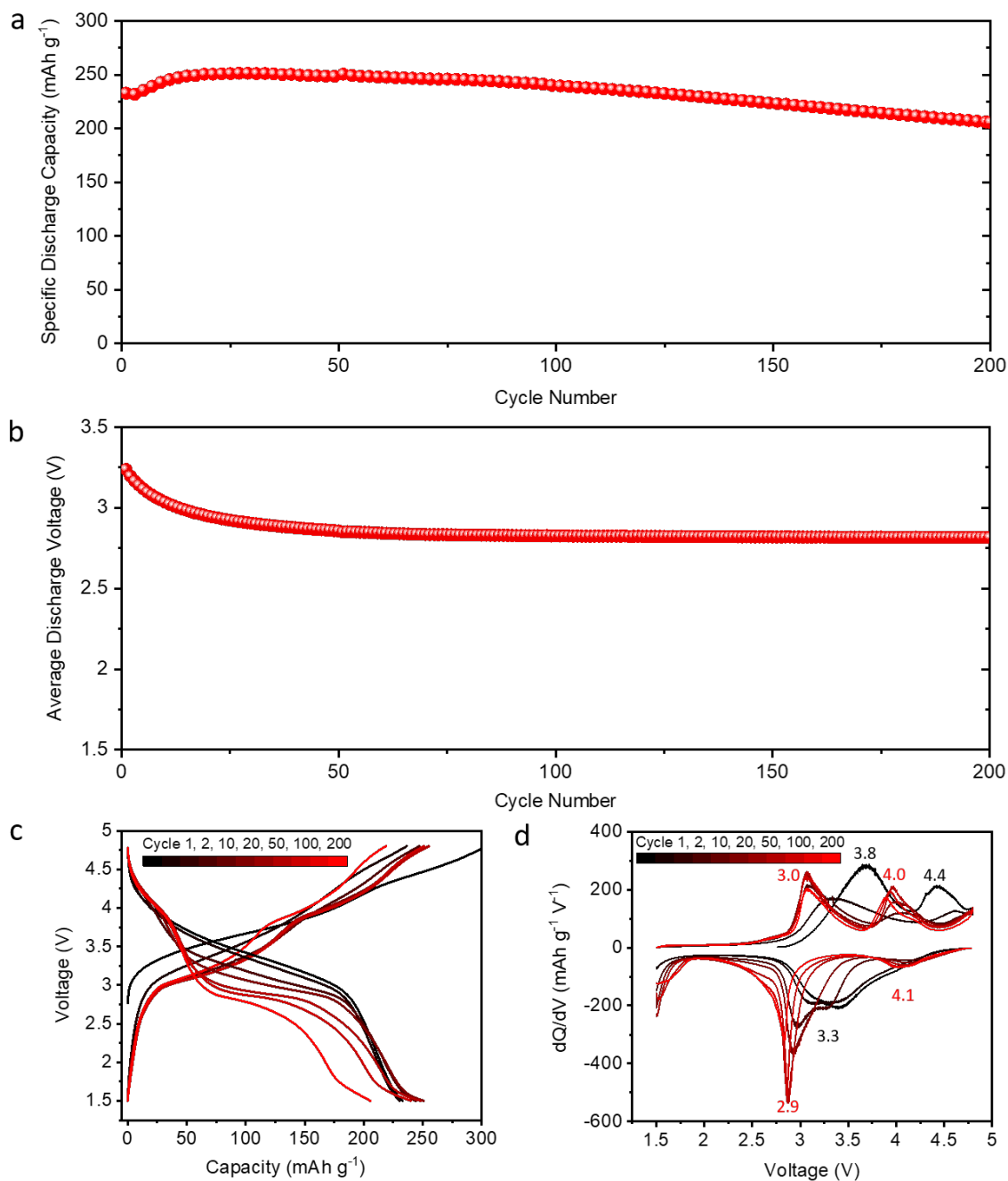
Figure 2. Electrochemical performance of LMTOF cathode. (a) Specific discharge capacity, and (b) average discharge voltage upon cycling, (c) selected charge-discharge voltage profiles, and (d) corresponding dQ/dV curves. LMTOF cell is cycled between 4.8 and 1.5 V at C/20.
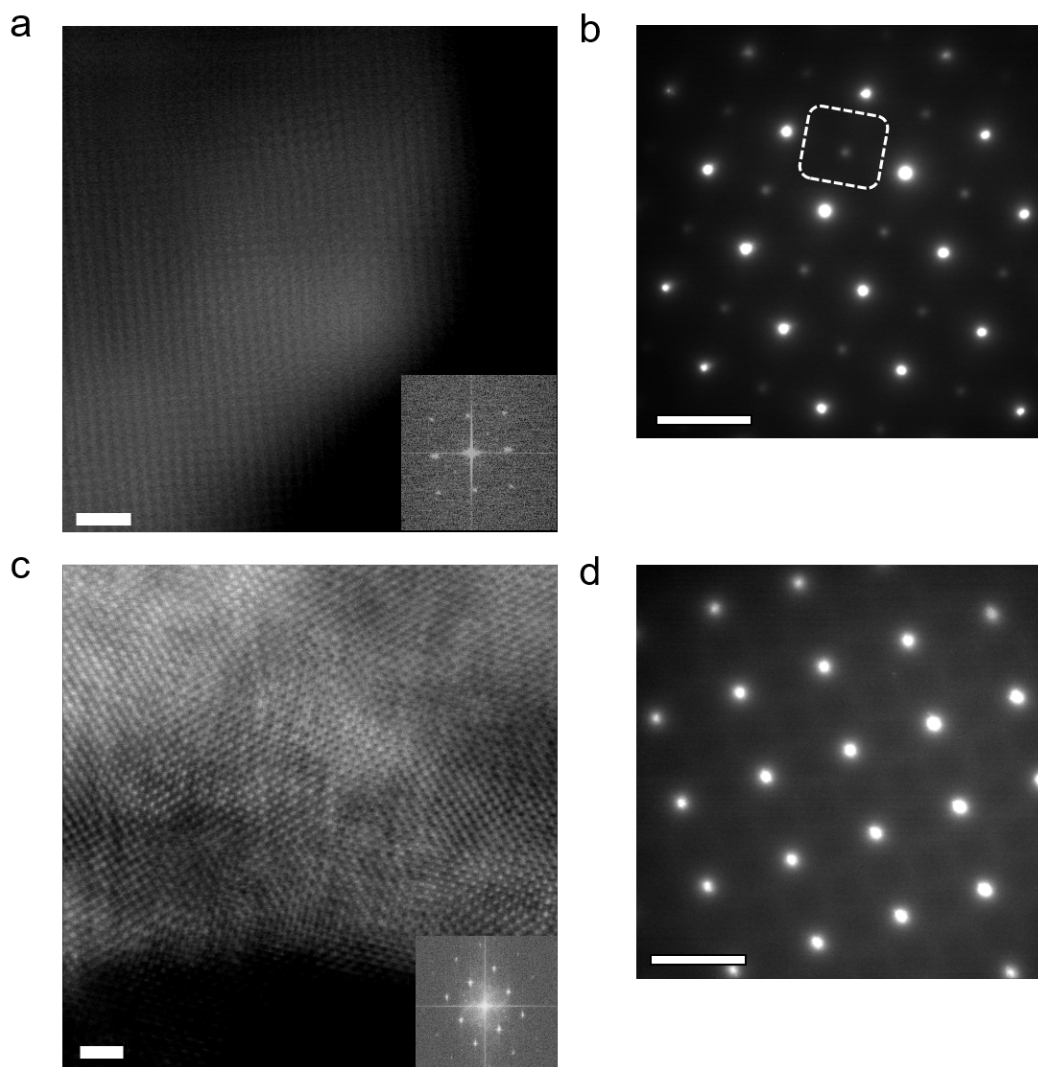
Figure 3. Structural evolution of LMTOF electrode upon cycling. (a) Representative HAADF-STEM image with FFT insert and (b) SEAD pattern after the 16th charge, the white box in (b) marks the diffraction spot corresponding to the spinel-like phase transformation; (c) representative HAADF-STEM image with FFT insert and (d) SEAD pattern after the 16th discharge. The scale bar in (a, c) and (b, d) is 1 nm and 5 nm^{-1}, respectively.
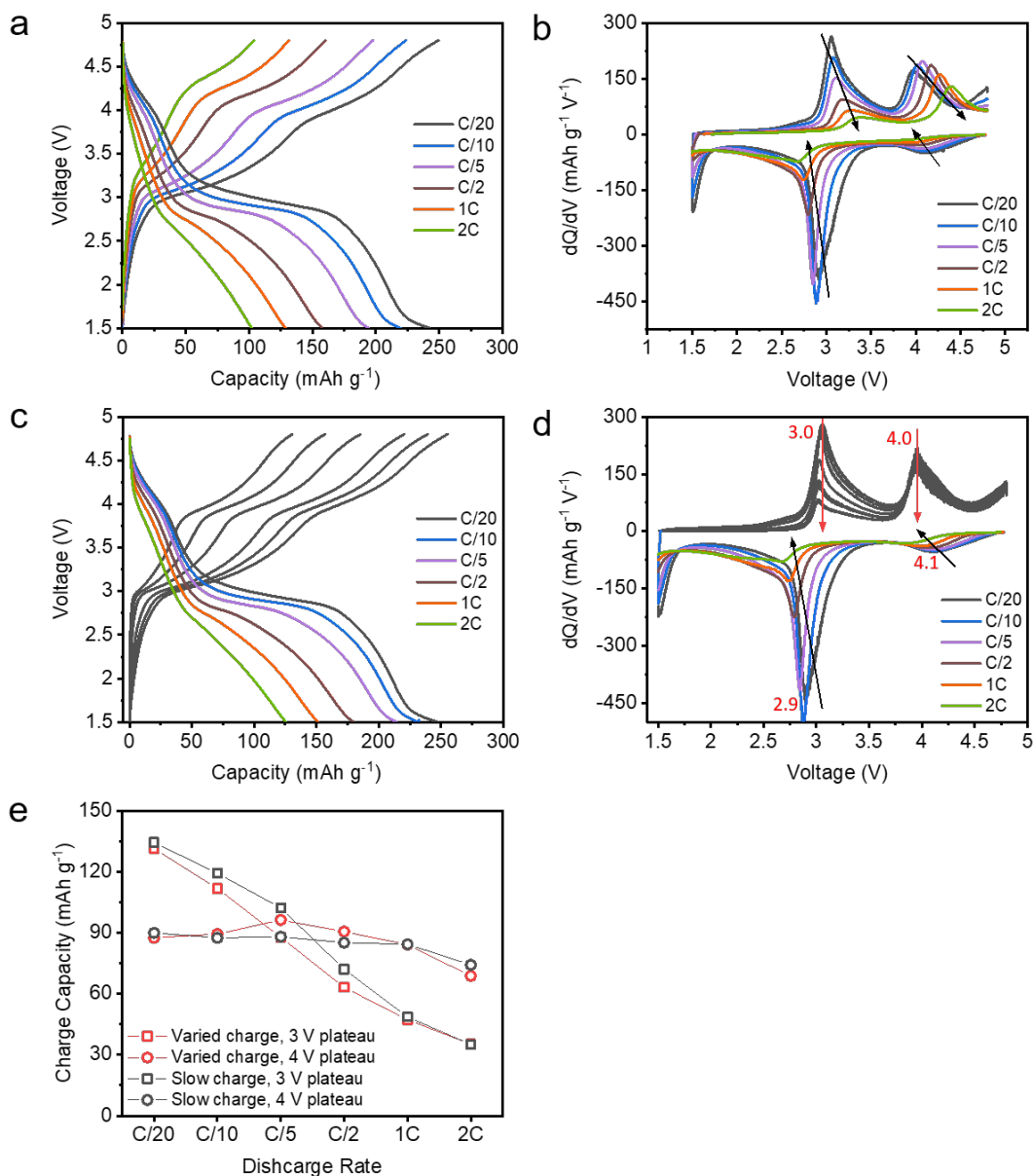
Figure 4. Electrochemical kinetics of LMTOF cathode after cycling. (a) Voltage profiles and (b) dQ/dV curves at varied charge-discharge rates, (c) voltage profiles and (d) dQ/dV curves at a slow charge rate of C/20 and varied discharge rates, (e) charge capacities at 3 and 4 V plateaus with different discharge rates, 3 V and 4 V charge capacities are calculated based on the voltages corresponding to the lowest values after 3 and 4 V presented in (b) and (d). Cells are previously subjected to an initial rate test and cycling test at C/20. All rate tests are conducted three times (curves are identical) and the third cycle is presented for analysis. Cells are cycled between 4.8 and 1.5 V. Black arrows indicate the change of oxidation/reduction peak with rate while red ones mark a strong contrast.
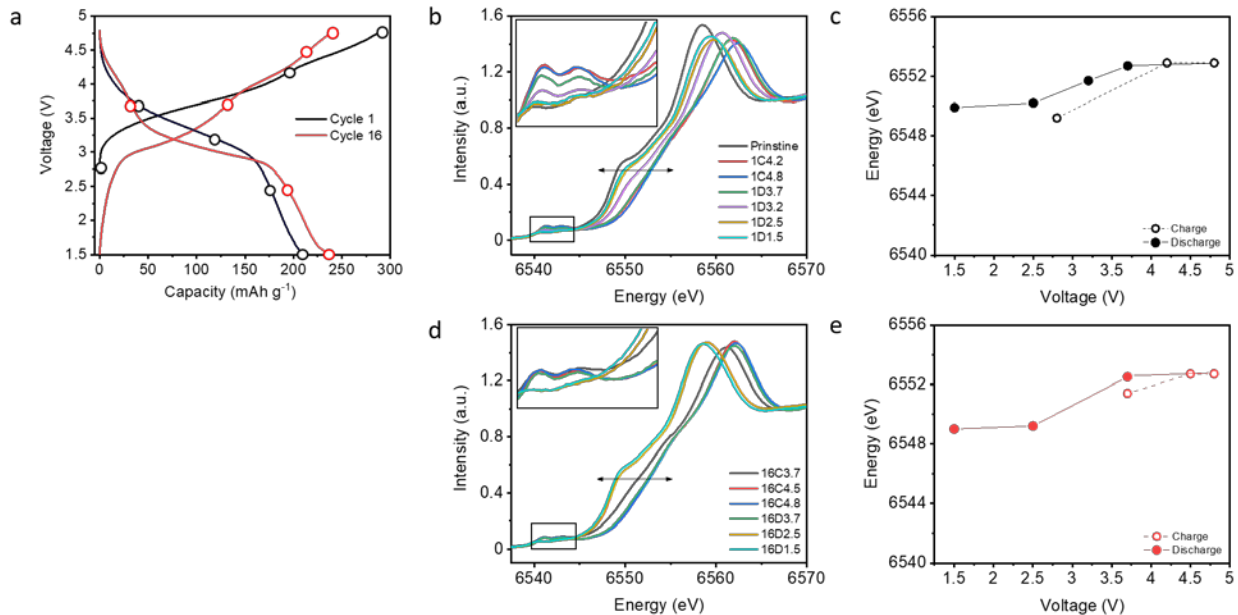
Figure 5. Chemical state of Mn during cycling of LMTOF cathode. (a) Selected states of charge during the 1st and 16th cycle, showing the effect of structural transformation upon electrochemical cycling, (b) Mn *K*-edge XANES and (c) corresponding half-edge energy during the first cycle, (d) Mn *K*-edge XANES and (e) corresponding half-edge energy during the 16th cycle. The insets in (b) and (d) are the enlarged Mn *K* pre-edge regions. Samples are labelled by the number of charge (C) or discharge (D) followed by the state of charge, e.g., 1C4.8 indicates the first charge at 4.8 V.
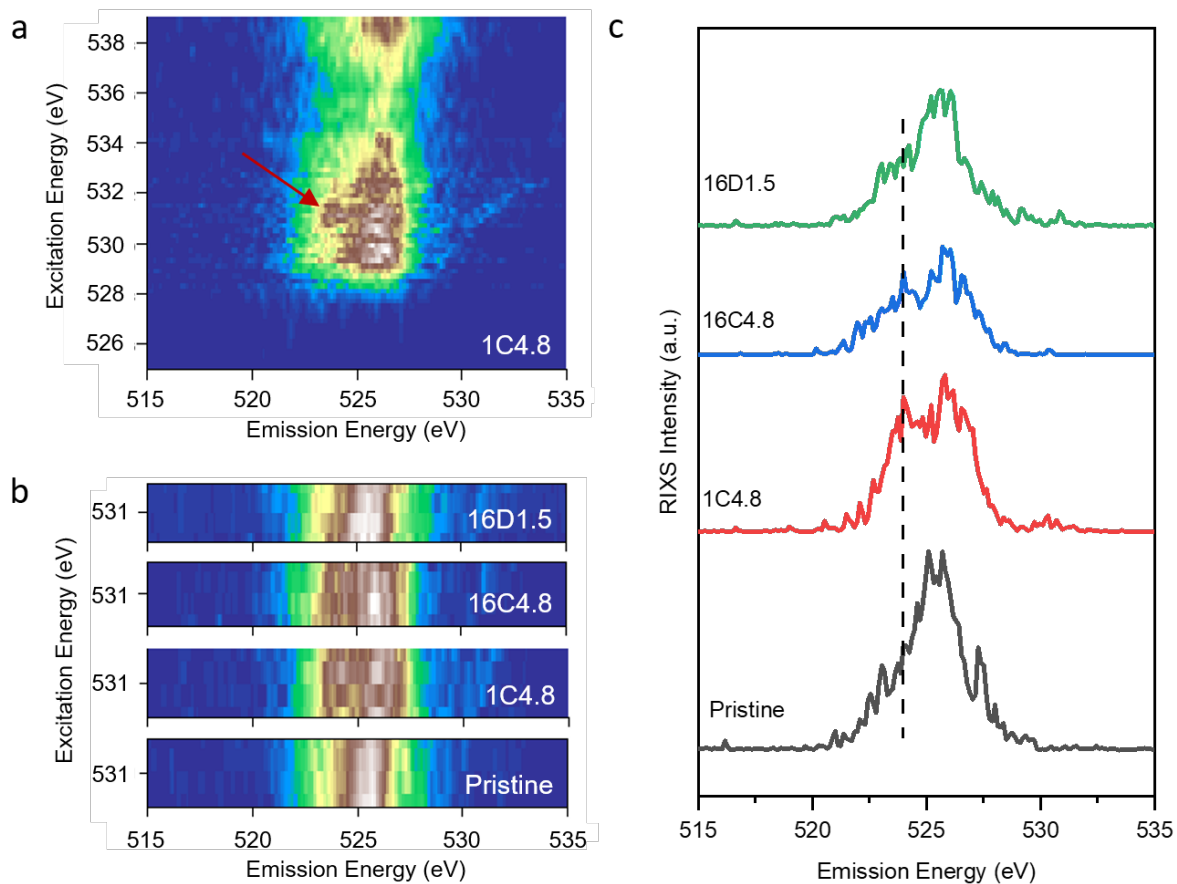
Figure 6. Chemical state of O during cycling of LMTOF cathode. (a) Full O *K*-edge RIXS map at the first charged state, red arrow indicates the O redox feature, (b) partial O *K*-edge RIXS maps and (c) corresponding O *K*-edge RIXS cut at 531.0 eV excitation energy at selected states of charge, the dashed line in (c) marks the O redox feature at 524.0 eV emission energy. Samples are labelled by the number of charge (C) or discharge (D) followed by the state of charge, e.g., 1C4.8 indicates the first charge at 4.8 V.

Supporting Information for

Toward Stable Cycling of Cost-Effective DRX Cathode via Fluorination

Ji Qian,[a] Yang Ha,[b] Wanli Yang,[b] and Wei Tong [a,*]

[a] *Energy Storage and Distributed Resources Division, Lawrence Berkeley National Laboratory, Berkeley, CA 94720 USA*

[b] *Advanced Light Source, Lawrence Berkeley National Laboratory, Berkeley, CA 94720 USA*
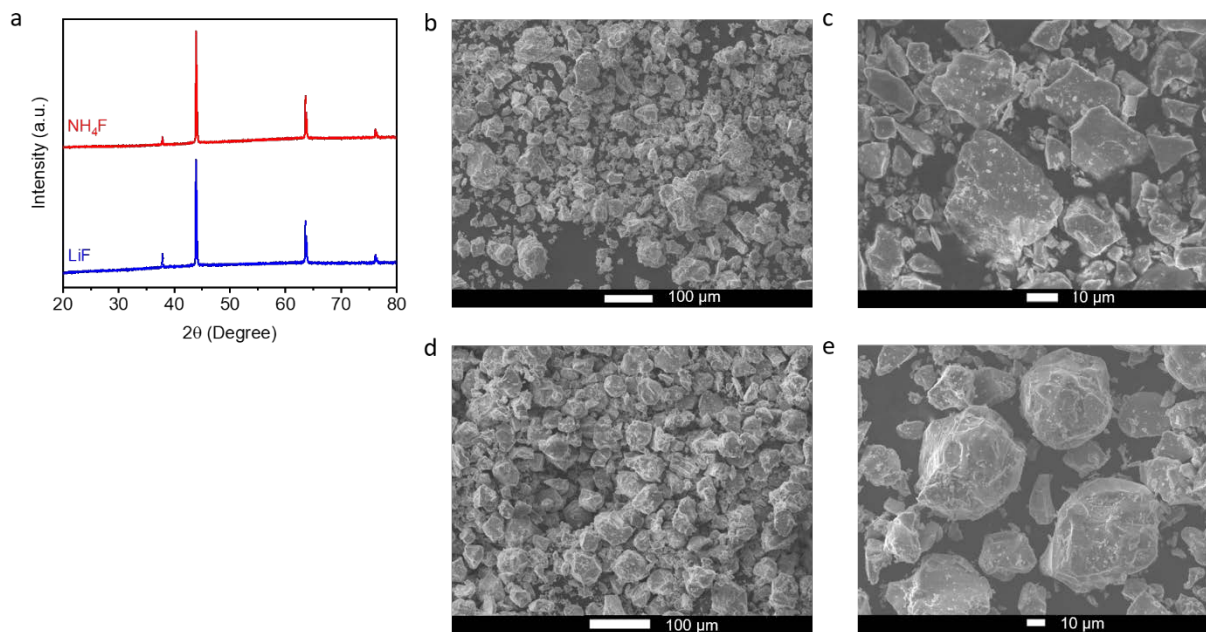
*Correspondence: weitong@lbl.gov

Figure S1. LMTOF cathodes prepared using LiF and NH$_4$F precursors. (a) XRD patterns, SEM images of LMTOF using (b, c) LiF and (d, e) NH$_4$F precursor. NH$_4$F leads to identical XRD pattern and more uniform particle size in the final product.
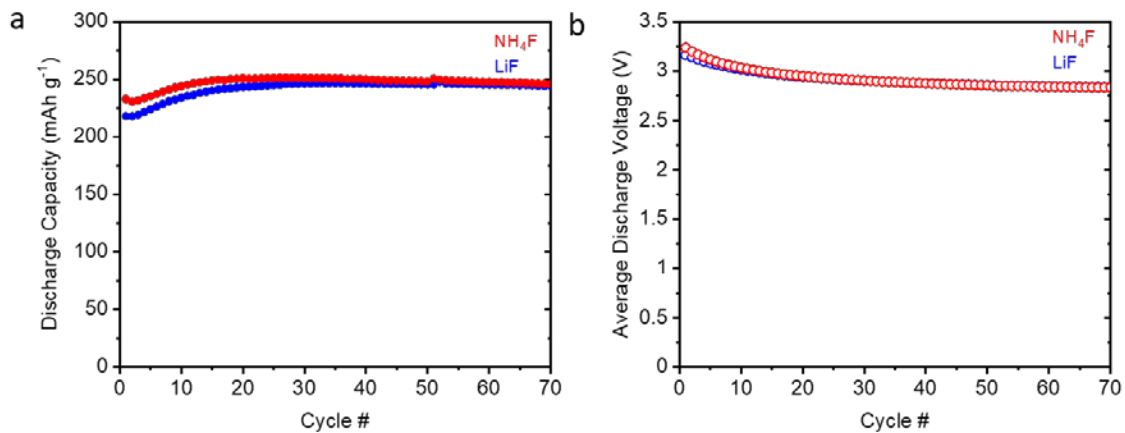
Figure S2. (a) Specific discharge capacity and (b) average discharge voltage of LMTOF cathodes using LiF and NH_4F precursors. The similar cycling performance indicates NH_4F is an effective F precursor.
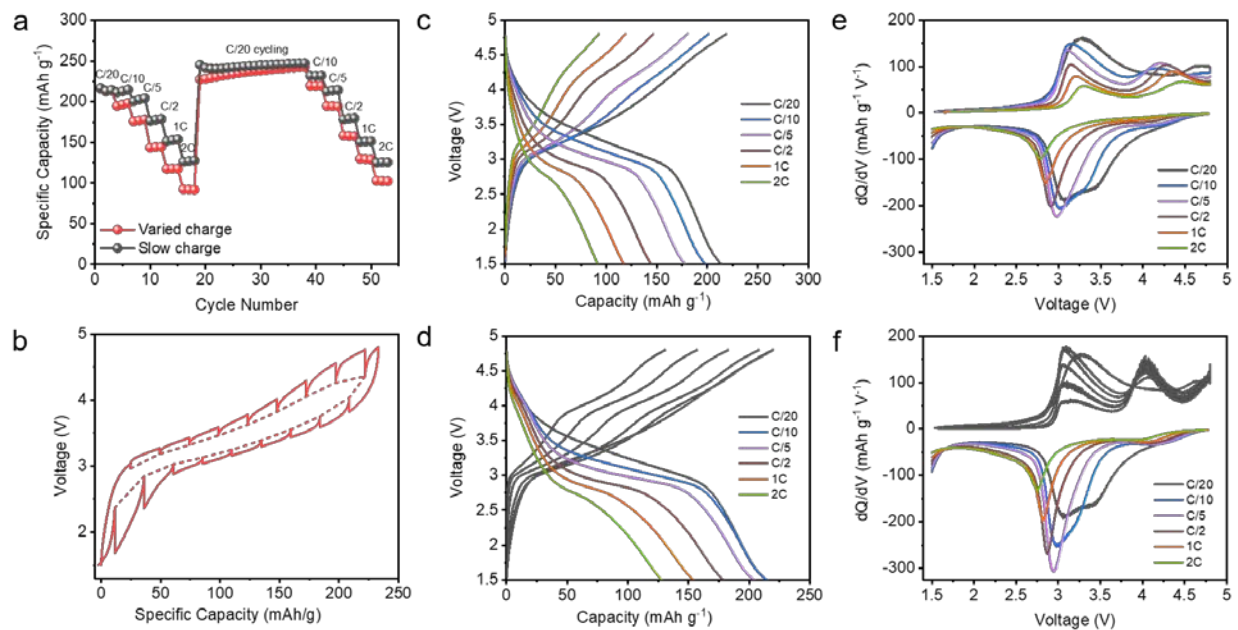
Figure S3. Electrochemical characterization of LMTOF cathode. (a) Overall cycling performance, red circles indicate the rate tests at the varied charge-discharge rates and black circles mark varied discharge rates but a slow charge of C/20, cycling between the rate tests is conducted at C/20 charge-discharge rate, (b) GITT curve, (c) voltage profiles and (e) dQ/dV curves at the varied charge-discharge rates, (d) voltage profiles and (f) dQ/dV curves at a charge rate of C/20 and varied discharge rates. Note (c-f) show the third cycle at each rate during initial rate test before cycling. Cells are tested between 4.8 and 1.5 V.